Check for updates

Synergetic and charge transfer properties of a metal oxide heterojunction: Photocatalytic activities

Buzuayehu Abebe*

Department of Applied Chemistry, Adama Science and Technology University, Adama, Ethiopia

Improvement in the synthesis techniques and their optimum properties to be up-to-date is the global need for industrially scalable applications. The sol−gel solution combustion synthesis (SG-SCS) approach is an easy, time-/energy-efficient, and creates regularly ordered porous materials that have significance in the ion-/mass-transport phenomenon. Furthermore, the approach also yields a decent heterojunction once optimized *via* the HSAB theory. Forming a heterojunction also tunes the crucial properties of the materials, thus, boosting the photocatalytic ability through charge transfer or/and synergistic roles. From the stability investigation results, the calcination temperature of 500°C is determined to be ideal. The X-ray diffraction and high-resolution transmission electron microscopy (HRTEM) techniques confirmed the nanoscale size of the NPs and NCs. The porous nature of the materials is revealed from the scanning electron microscopy micrographs and BET analysis; consistent results are also noted from selected area electron diffraction and HRTEM. The detected stacking faults on the IFFT image of HRTEM also confirmed the porous properties of the NCs. The precise elemental composition and local heterojunction within Zn/Fe(III)/Mn(III) oxides were confirmed in the HRTEM, X-ray photoelectron spectroscopy, and energy-dispersive X-ray studies. The significant charge transfer capability of the NCs more than bare ZnO was evidenced from the electrochemical analysis. The NCs were also effective on acid orange 8 (AO8) and Congo red (CR) dye degradations.

KEYWORDS

solution combustion synthesis, nanocomposites, photocatalytic degradation, mechanism, dyes

Introduction

With the fast expansion of industries across the globe, ecological care is the current anxiety. Previously, several physicochemical approaches were adapted for the remediation of toxic and non-biodegradable contaminants (Adeleye et al., 2016; Pype et al., 2016). Among the adapted remediation techniques, heterogeneous photocatalysis was justified to be very simple and degraded pollutants without creating any secondary pollution

(Gómez-Pastora et al., 2017). Semiconductor metal oxides have unique chemical and physical properties for different applications (Nagvenkar et al., 2019). Comparable to TiO$_2$, zinc oxide NPs (ZnO NPs) have received significant attention (Janotti & Van de Walle, 2009). A proper heterojunction inhibits photo-induced electron–hole recombination through the charge transfer process (Lachheb et al., 2017), which is important for the photocatalytic degradation of dyes.

Several recent works reported material stability and surface area improvement through the synergistic effect and charger transfer role through the heterojunction/hybrid (Saravanan et al., 2014; Lachheb et al., 2017; Chen et al., 2021; Srinivasa et al., 2021). (Dhal et al., 2015) synthesized ternary Fe$_2$O$_3$/ZnFe$_2$O$_4$/ZnO NCs materials by using hydrothermal methods for the degradation of malachite green dye. The ternary NCs show a greater photocatalytic activity than the parent α-Fe$_2$O$_3$ material due to the presence of cascade electron transfer. The effective charge transfer properties from ZnO to α-Fe$_2$O$_3$ were also confirmed in (Uma et al., 2020) studies based on the electrochemical impedance spectroscopic analysis. The step-scheme-type of charge transfer from the Fermi level of ZnMn$_2$O$_4$ to ZnO, which was confirmed by photoluminescence spectroscopy, was recently reported a in study (Deng et al., 2021). Lam et al., 2021 also synthesized MnO$_2$/ZnO nanocomposites for methyl green dye degradation The MnO$_2$ distributed on the surface of ZnO nanoflower composites showed greater degradation activity due to the presence of an accelerated charge transfer. Saravanan et al., 2015 synthesized ZnO/Ag/Mn$_2$O$_3$ NCs by using the thermal decomposition method as the degradation of industrial textile effluent. Compared to the parent ZnO NPs, the NCs here also showed an improved photocatalytic activity. In this study, the photocatalytic enhancement is reported to be due to the Mn$_2$O$_3$ and Ag synergistic surface area improvement and charge transfer behavior within the NCs that in turn reduces the electron–hole recombination process. The electron transfer occurred from ZnO to Mn$_2$O$_3$ and Ag (Ag which acts as an electron reservoir). N (Li et al., 2020) also developed an interface within the Mn$_3$O$_4$@ZnO/TiO$_2$ NCs and confirmed the presence of an electron and hole transfer within the interfaces. Here in, the positive position, an XPS peak shift for the NCs than the parent ZnO is used to interpret the transfer process of an electron in the cascade form (from Mn$_3$O$_4$ to ZnO, and then to TiO$_2$). The holes transferred from TiO$_2$ to ZnO, and then to the Mn$_3$O$_4$. In general, the aforementioned reports show that, compared to the parent and binary materials, forming a ternary heterojunction raises the materials' synergistic and charge transfer properties.

However, for successful heterojunction, the host-dopant reactivity based on Pearson's hard/soft acids/bases (HSAB) theory is the base. According to the HSAB theory, hard Lewis acids [such as Mn(III) and Fe(III)] cannot diffuse into the borderline Zn (II) host lattice in a hard base solvent like water (Buonsanti & Milliron, 2013; H. Hu et al., 2018).

Preferably, they adsorbed on the host surface and oxidized to form a hybrid/heterojunction upon calcination.

Among several bottom-up wet chemical methods, the sol–gel-based solution combustion synthesis (SG-SCS) approach has been reported to be efficient in time and energy and for creating mass/ion transport active well-defined porous nanomaterials (Deganello and Tyagi, 2018). The SG-SCS approach is an effortless, time-/energy-efficient method, which is valid for industrially scalable applications (Deganello and Tyagi, 2018). SG-SCS is an exothermic reaction process, which occurs between reducers/organic fuel and oxidizers/metal nitrates. The salt oxidizers can be reducers, neutrals (chlorides), or oxidants (nitrates). The reducer-based precursor needs oxidants such as NH$_4$NO$_3$ and HNO$_3$. Neutral/chlorine-based precursors release HCl, resulting in the contamination of the final products. Thus, the oxidants (nitrates) are the best oxidizers due to their better oxidizing potential, stable decomposition temperature (Kim et al., 2014), and noble solubility (Zhang et al., 2012). The properties mentioned previously are also related to the metal–cation charge density, exchange kinetics, and the cations' standard molar Gibbs free energies of hydration (Yuvaraj et al., 2003; Cochran et al., 2019).

The SG-SCS follows 1) colloidal/sol formations, 2) gel formation by evaporating the water molecules, 3) locally activated combustion reaction (Khort et al., 2021; Novitskaya et al., 2021), 4) propagation along the rest of the media, and 5) finally, the quenching of the reaction by the evolution of gases. Of course, the by-product may further react to the reducing gases/atmosphere and result in a metal reduction. The evolution of gases improves the porosity/textural properties of the product (González-Cortés and Imbert, 2013). In SG-SCS, the combustion processes may start from many points, resulting in a porous/foam-like structure, or it starts at one spot/point that forms a long wire metal oxide (Gao et al., 2016; Nersisyan et al., 2017). Moreover, due to the high surface energy and prominent surface area of metal oxide NPs, they possibly aggregate through the continuous electron–hole quenching (Jassby et al., 2012). For the aggregation problem, polymers are one of the real choices to be used as a stabilizing and structure-directing tool (Wu et al., 2016).

Here in this work, the poly (vinyl alcohol)-assisted ZnO NPs and ZnO-based binary and ternary NC heterojunctions are successfully synthesized. An environmental-friendly SG-SCS approach was used with PVA complexing and stabilizing agents. The ZnO host with Fe(III) and Mn(III) oxide heterojunctions was estimated based on the HSAB theory. As far as the author's knowledge is concerned, forming a zinc–iron–manganese oxide ternary-based heterojunction based on the HSAB reactivity selection theory and using the decent solution combustion synthesis approach is the first work. The heterojunction plays a vital role in charge transfer; consequently, the synergistic characters act as an electron–hole recombination-reducing agent. The current

SCHEME 1
The schematic diagram shows the polymer-assisted SCS that creates porous NP and NC materials. **(A)** precursor decomposition using heat and stirrer; **(B,C)** sol and gel formations upon dehydration at 110°C; **(D)** the combustion process heating to the ignition temperature of the complexes formed; **(E)** calcination at DTG-optimized temperature of 500°C; **(F)** porous by-products formed as a result of gas evolution.

analytical characterization techniques have been utilized to realize the structural, optical, and morphological properties. The degradation efficiency of NPs and NCs has been tested on highly stable and toxic CR and AO8 dyes. The ternary NCs showed a good photo-degradation activity for both CR and AO8 dyes than the parent ZnO NPs. Therefore, the ternary-based heterojunction is a appreciable method for improving a material's properties and dye degradation abilities.

Materials and methods

Synthesis of NPs and NCs

The details of the chemicals and analytical techniques are incorporated as supplementary materials (S). The ZnO NPs were synthesized using an environment-friendly sol–gel approach. A 10 mM aqueous solution of the zinc nitrate precursor has been prepared by adding a stoichiometric amount of salt in 100 ml of distilled water. The obtained colloidal particles of the metal hydroxide were aged for nearly 2 days. Then, the solution was dehydrated in an oven at ~110°C for 8 h and further calcined at 500°C for 3 h.

The binary and ternary nanocomposites were synthesized using the poly (vinyl alcohol), a surfactant; also a complexing agent-assisted SG-SCS approach. To synthesize the binary Zn-Fe oxide NC, the PVA polymer solution was initially dissolved in distilled water (at 115°C) with constant stirring for 20 min (Liu B

et al., 2016). Then, the zinc nitrate $(Zn(NO_3)_2.6H_2O)$ and iron nitrate $(Fe(NO_3)_3.9H_2O)$ salt precursors were added to the previously dissolved PVA solution with continuous stirring. The developed colloidal particles of the metal hydroxide were aged for 2 days and dehydrated at 110°C to form a dense result. Then, it was further combusted to its ignition temperature and ignited at 500°C for 3 h (Scheme 1). Following the same protocol, the other Zn-Mn binary and Zn-Fe-Mn ternary metal oxide NCs were also synthesized. The synthesized Zn-Fe and Zn-Mn binary metal oxides using PVA (PBNCs) denoted PB1 and PB2. The synthesized PVA-aided ternary NCs (PTNCs) were coded as PTP1.

Batch degradation studies

The batch degradation tests took 20 ppm of CR and AO8 dyes in a 0.25 L aqueous solution with 60 mg of NPs and PB1, PB2, and PTP1 NCs. To create the adsorption/desorption equilibrium of AO8/CR dyes on the NPs/NCs, the mixture was stirred constantly in the dark for 30 min before illumination. The temperature of the overall reactor was controlled by water circulation and with a wind fan. The experiment was conducted in a circular glass reactor in the presence of a mercury vapor lamp. The concentrations at time t were measured by withdrawing 5 ml of the solution every 15 min. The dye degradation effectiveness of the photocatalyst was calculated using Supplementary Equation S2. The PFO

FIGURE 1
Thermal analysis: TGA/DTA plots of **(A)** PTP1, **(B)** PB1, and **(C)** PB2 before calcination.

FIGURE 2
Structure and crystallinity analysis: XRD patterns for PVA, ZnO NPs and PB1, PB2, and PTP1 NCs calcined at 500°C.
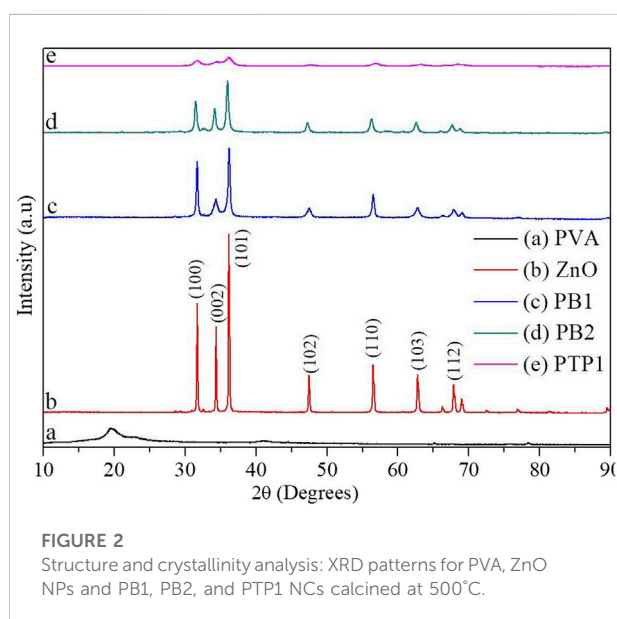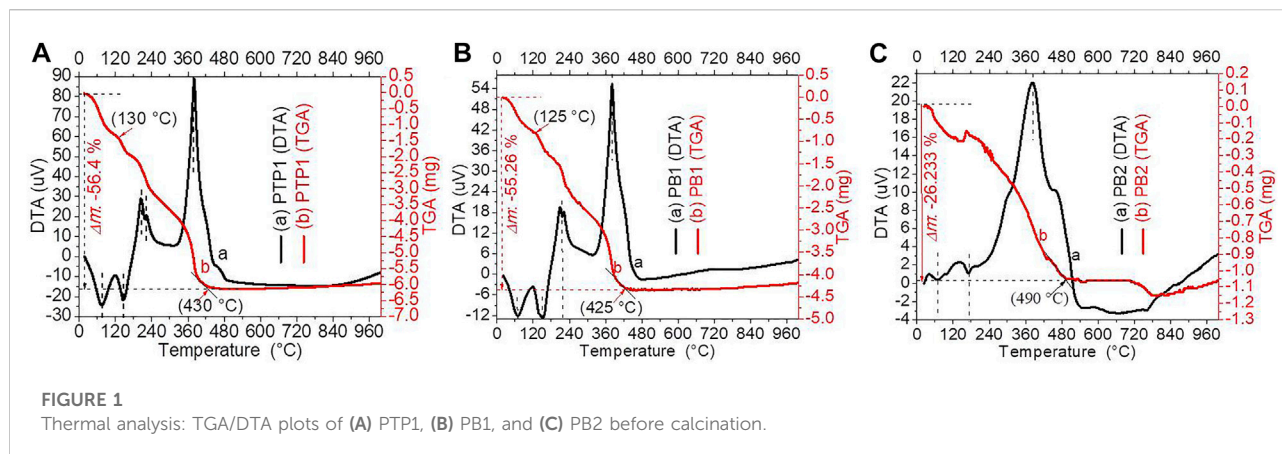
kinetic equation (Supplementary Equation S2) was adapted to study the reaction mixture dynamics.

Results and discussion

Characterization

Figure 1 depicts the thermal stabilities of PB1, PB2, and PTP1 NCs before calcination analyzed by a DTG instrument in an N_2 atmosphere. A sequence of vaporization of adsorbed H_2O molecules, intramolecular decay, metal hydroxides, or/and polymer side chain decompositions, main chain decomposition/intermolecular, and finally, the crystalline part decompositions occurred to give hydrocarbons, carbon, and ash (Dai et al., 2018; S. Kumar et al., 2019; Radhamani et al., 2016).

The corresponding approximate decomposition temperature ranges for PTP1 NCs were found to be 40°C–120°C, 120°C–180°C, 180°C–220°C, 220°C–280°C, and 280°C–430°C (Figure 1A) (Singh and Dutta, 2019). Figures 1B, C show the DTG analysis for the PB1 and PB2 NCs, respectively. Except for a slight decomposition temperature (<5°C) and stability differences, the PB1 NC has nearly similar decomposition steps to PTP1 NC. Between the temperature ranges of 500°C and 900°C, the PTP1 NC showed better stability than the PB1 NC. The PB2 NC decomposition temperature step also has similarities to the PB1 and PTP1 NCs, although there is a high stability loss between 500°C and 900°C.

Figure 2 shows the x-ray diffraction pattern, which confirms the crystallinity and phases of single PVA, ZnO NPs, PBNCs, and PTNCs. Inset label (b) of Figure 2 shows the angles of diffraction with their corresponding crystal planes [~32°(100), 34°(002), 36°(101), 47°(102), 57°(110), 63°(103), 66°(200), 68°(112), 69°(201), 73°(004), and 77°(202)], which are in agreement with the ZnO NPs [hexagonal structure, space group P63mc (ICSD: 00–036-1451)]. The crystal structures of ZnO, Mn_2O_3, and Fe_2O_3 were created by VESTA 3D imagining program software (Figures 2B–D). The approximate crystallite size values for PB1, PB2, and PTP1 are 29, 23, and 10, respectively. The XRD data and the respective crystallite sizes were calculated using Scherrer's equation (Supplementary Equation S3). The XRD pattern peak width has a close relationship with the size of the crystallite; the broader the full width at half maximum, the lesser the crystallite size.

The XRD peaks of both ZnO NPs and NCs confirmed the hexagonal crystal phase of ZnO. The absence of peak shifts for NCs relative to ZnO shows the non-appearance of structural alterations on the ZnO d-spacing ascribed to Mn^{3+} or/and Fe^{3+} ion infusion. Thus, iron oxide and manganese oxide NPs exist as distinct phases by creating local heterojunctions with ZnO (Lachheb et al., 2017). Actually, as expressed in the HSAB hardness theory, hard Lewis acids cannot diffuse into the host lattice; instead, they are adsorbed on the surface and oxidized to

FIGURE 3
(A) Textural properties analysis: the BET plots of ZnO NPs and PB1, PB2, and PTP1 NCs (Inset: the respective Barrett−Joyner−Halenda pore size distribution plots). **(B)** Chemical bonding analysis: FT-IR spectra of ZnO NPs, PB1, PB2, and PTP1 NCs calcined at 500°C.
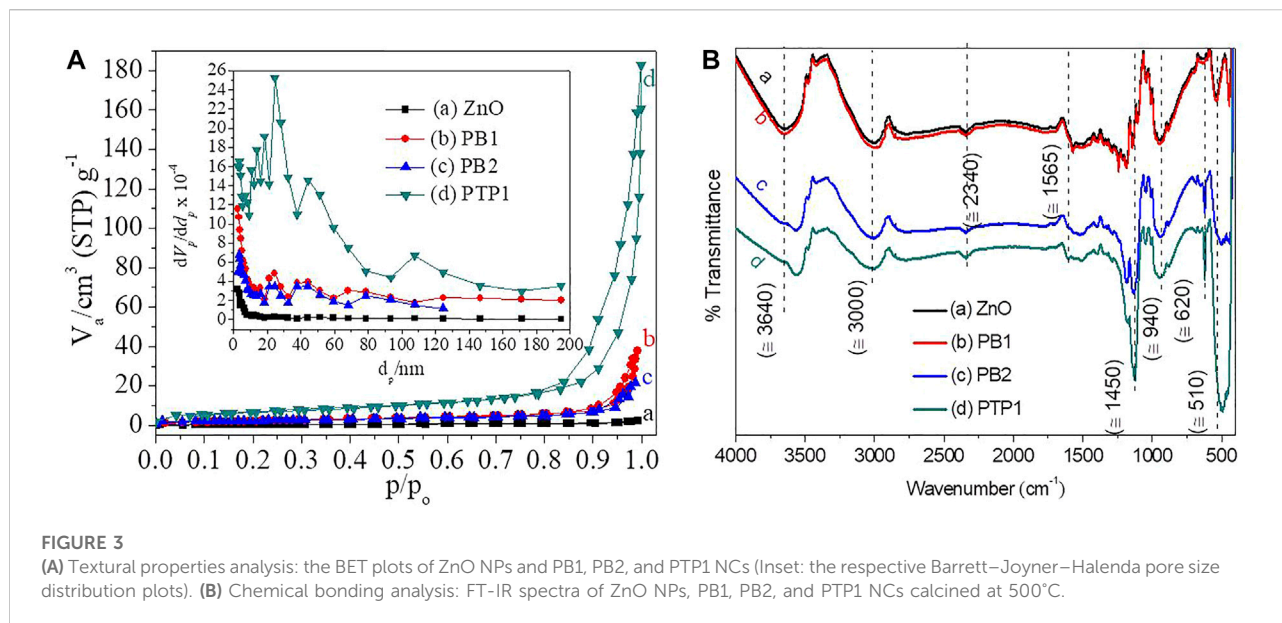
form a hybrid upon calcination (Buonsanti and Milliron, 2013; Hu et al., 2018). The XRD peaks of PVA were not observed in the XRD patterns of binary and ternary NCs; it indicates the total decomposition of the polymer at 500°C, as validated in the TGA/DTA result. The PTP1 NCs showed enhanced SAS compared to ZnO NPs and the two binary metal oxide NCs. In conclusion, the overall XRD results of NPs and NCs have confirmed an enhancement in SAS for the NC materials.

Enhanced SAS and SSA of the NPs/NCs have a significant interest in diverse applications. For measuring the SSA of porous nanomaterials, the BET technique at 77 K is operative (Rosman et al., 2019). The BET plots of ZnO NPs, PB1, PB2, and PTP1 NCs are shown in Figure 3A. Among the basic pore shape models including ink-bottled, slit shapes, and cylindrical (Broekhoff and Issue, 1979; Thommes et al., 2015), the synthesized NPs and NCs look like cylindrical shapes. The BET adsorption isotherm linear equation that fits linearly within the relative pressure of 0.5 and 0.35 (Boningari et al., 2018) is shown in Supplementary Equation S4. One can calculate the slope, intercept, and monolayer capacity n_m from the linear plot. Then, using the obtained n_m value, SSA can be calculated *via* Supplementary Equation S5. From the linear equation, the value of C can also give pieces of information about the shape of the isotherms. Suppose the value of C is greater than 80. In that case, a sharp knee occurs, and the isotherm becomes more acceptable, <50 indicates the existence of multilayer and monolayer adsorption overlays, and <2 shows Type III or Type V adsorption isotherms (Thommes et al., 2015).

According to the IUPAC classification, there are six adsorption isotherms and four hysteresis loop types (Kumar et al., 2016). The appearances of the synthesized NPs and NCs have been matched with the IV adsorption isotherm and

H3 hysteresis loops. The sharp increase at the p/p_o value of 0.8 substantiates the co-occurrence of both mesopore and macropore pore sizes (Liu J et al., 2016). The pore size distribution of the porous material is expressed in terms of the BJH curvature by considering the microporous, mesoporous, and macroporous natures with their respective <2.0 nm, 2.0–50.0 nm, and >50.0 nm pore size distributions into consideration (Thommes et al., 2015). The approximate average pore size distribution of the synthesized NPs and NCs was observed to be between 10 and 45 nm, which corroborated the domination of the mesoporous pore size distribution. As seen from Figure 3A inset, a pore size distribution higher than 60 nm shows an insignificant macroporous pore distribution (Liu J et al., 2016). Compared to ZnO NPS, the PBNCs and PTP1 showed an enhanced SSA and optimized pore volume.

The FTIR spectra of ZnO NPs and PB1, PB2, and PTP1 NCs, which give information about the chemical bonding features of the materials, are given in Figure 3B. The absorption band appeared at 3,650 due to the hydroxyl group stretching and at 1,630 cm^{-1} assigned to the water molecules stretching. The semiconductor metal oxide exhibits a transverse optical stretching mode causing a band below 1,000 cm^{-1} (Wu et al., 2010). These absorption peaks were associated with the transverse-optical and longitudinal-optical phonon frequencies (Z. Yang et al., 2010). The morphological, compositional, and structural features of the NPs and NCs possibly influence the number and position of the peaks. Morphological modifications from the spherical dimension to one-, two-, or three-dimensional particles are believed to cause broadness and splitting of the bands (Sigoli et al., 1997; Fatehah et al., 2014). For the highly crystalline ZnO NPs, the absorption peaks were divided into two
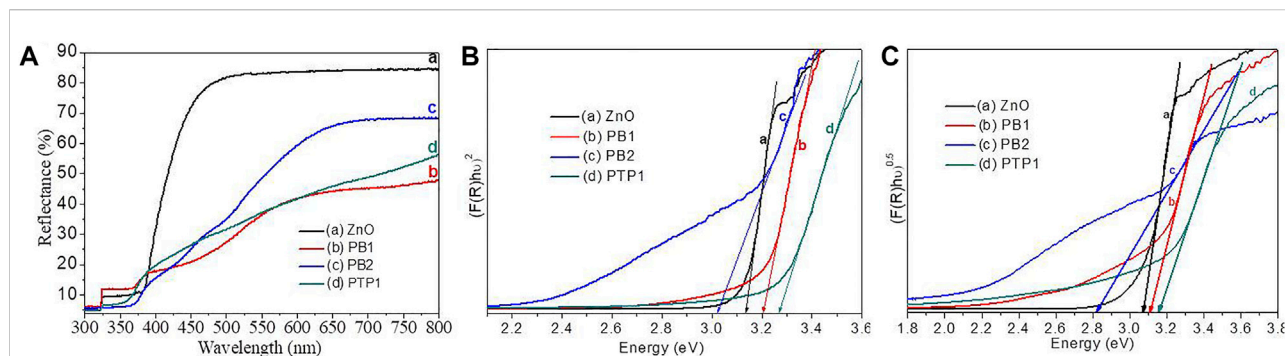
FIGURE 4
Optical properties analysis: **(A)** DRS plots. **(B)** and **(C)** the direct and indirect Kubelka−Munk plots of ZnO NPs and PB1, PB2, and PTP1 NCs calcined at 500°C.
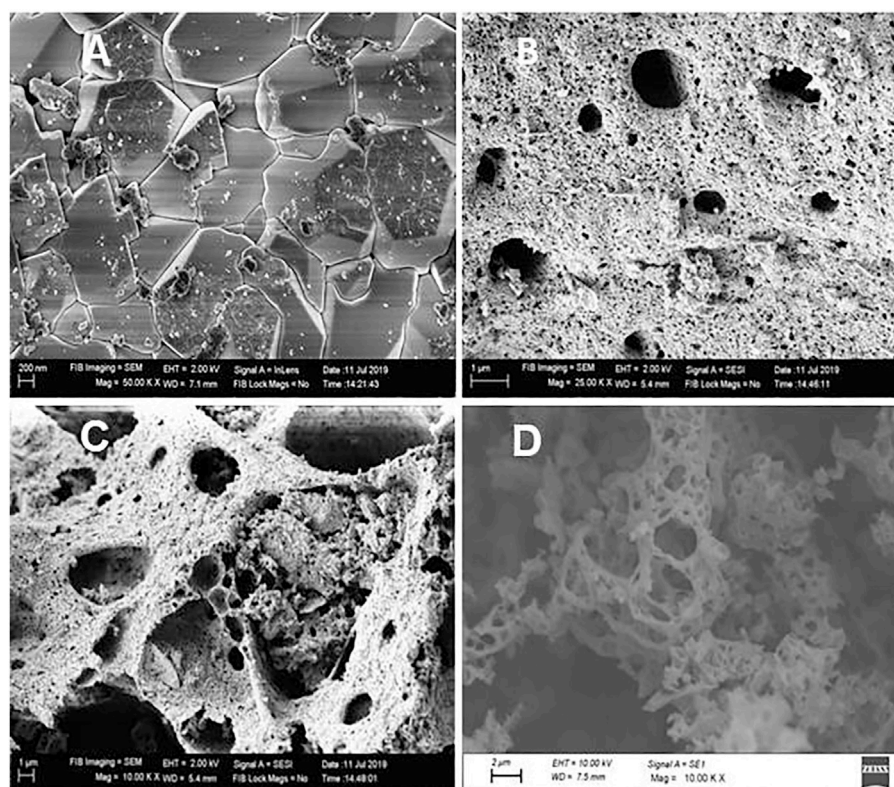
FIGURE 5
Morphological analysis: the SEM images **(A)** ZnO NPs, **(B)** PTP1, **(C)** PB2, and **(D)** PB1 NCs.

parts, while for the NCs, only one peak at about 450 cm^{-1} was observed. The presence of an irregular morphology for ZnO NPs and a spherical morphology for NCs has been confirmed from the SEM image analysis. The difference in peak position and peak number has been noticed between the ZnO NPs and NCs. The wave number shift is also dependent on the strength and

weakness of the metal–oxygen bond (Wachs, 1996). There are peak shifts toward a lower wavenumber/frequency for PB2 and PTP1 (3560 cm^{-1}) compared to ZnO and PB1 (3655 cm^{-1}). It shows that the introduction of the Mn$_2$O$_3$ phase was weakening the metal–oxygen bond (Parler et al., 2001). The DTG analysis also confirmed the less stable properties of PB2. All the other
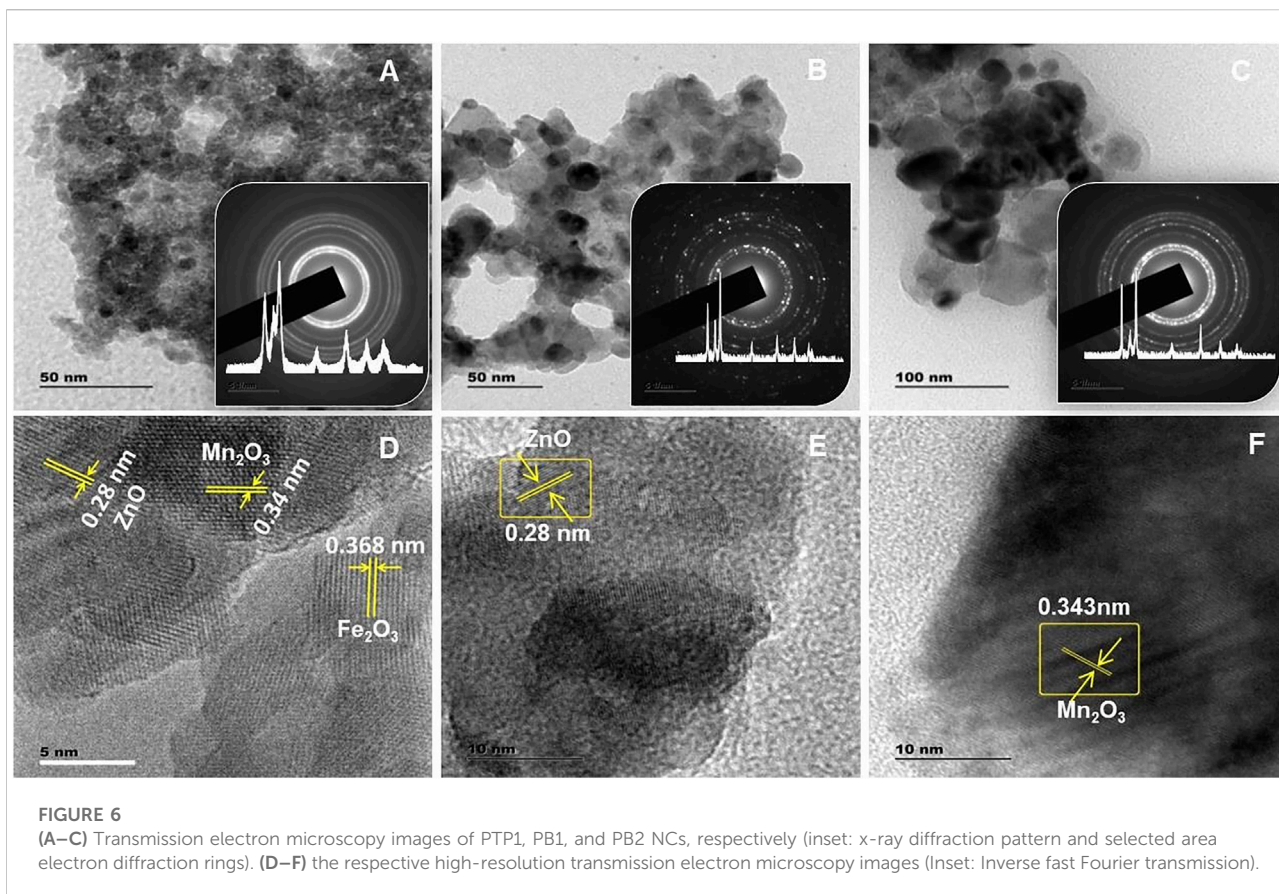
FIGURE 6
(A–C) Transmission electron microscopy images of PTP1, PB1, and PB2 NCs, respectively (inset: x-ray diffraction pattern and selected area electron diffraction rings). **(D–F)** the respective high-resolution transmission electron microscopy images (Inset: Inverse fast Fourier transmission).

peaks could have appeared due to the transitional impurities produced during synthesis (Anžlovar et al., 2011).

The UV–vis–DRS spectroscopy analysis was utilized to understand the optical behavior of the synthesized ZnO NP and NC powders (Figure 4). The material's per cent reflectance versus wavelength plot exhibited a distinct absorption edge near 380 nm (Figure 4A). The Kubelka–Munk (KM) function of single ZnO NPs and PB1, PB2, and PTP1 NCs are given in Figures 4B, C, respectively. Compared to the NCs, pure ZnO NPs showed less absorbance in the visible region due to their broader bandgap energies (3.17 eV). The PB1 and PTP1 NCs have low reflectance (~45%) compared to ZnO NPs. This improved absorbance behavior of the NCs is ascribed to the surface material's imperfect/porous nature (Nsib et al., 2015), as confirmed by the SEM and BET analyses. For semiconductor materials, the absorption coefficient α and the band energy E_g can be correlated by Supplementary Equation S6. From the remission function of Supplementary Equation S6 and using Kubelka–Munk scattering coefficient S as a constant, Supplementary Equation S7 can be derived. The direct and indirect E_g values of ZnO NPs and PB1, PB2, and PTP1 NCs were measured by extrapolating the KM plot's linear portion (Figures 4B,C). No obvious bandgap change has been detected except for PB2 NC-indirect Kubelka–Munk

plots. Compared to the single ZnO NPs, the recorded small shift toward lower wavelength (blue shift) for the PTP1 NCs can be ascribed to the confinement effects (Shah et al., 2014).

The SEM images of ZnO, PB1, PB2, and PTP1 NCs are revealed in Figures 5A–D. For the absorption of pollutants and photocatalysis, gas sensors, and as an electrode, the high porosity and high SSA, provide sufficient active sites unusually compared to the solid structures. The SEM images of PTP1, PB1, and PB2, showed better porosity. The compositional analysis by using the EDX technique verified the reality of the predictable Zn, Mn, Fe, S, and O elemental compositions in all BNCs and TNCs (Supplementary Figures S1A–C). For PTP1, PB1, and PB2, the main peaks at 1/2, 1, and 6.5 keV were assigned for Mn, Zn, and Fe, respectively. However, S, Cl and N, and C and S were detected as impurities in PTP1, PB1, and PB2 NCs. The source for S, Cl, N, C, and S impurities is assumed to come from the precursors used.

The HRTEM, SAED, and d-spacing analyses conducted for PTP1, PB1, and PB2 NCs are given in Figures 6A–C. From the TEM images, the sizes of the synthesized NCs were in the nanometer range (~10–70 nm); this is consistent with the XRD analysis. From the TEM images, it is also possible to visualize the existence of twins separated by boundaries between NPs, which is known as an oriented attachment (Penn, 1998). This attachment allows the particles to share a

FIGURE 7
Electrochemical properties analysis: **(A–D)**. CV plots of ZnO NPs, PTP1, PB1, and PB2 NCs electrodes at different scan rates, respectively. **(E–G)** EIS plots of PTP1, PB1, and PB2 NCs, respectively. **(H)** the combined EIS spectra for ZnO, PB1, PB2, and PTP1 NCs (Inset: their magnified EIS plots).
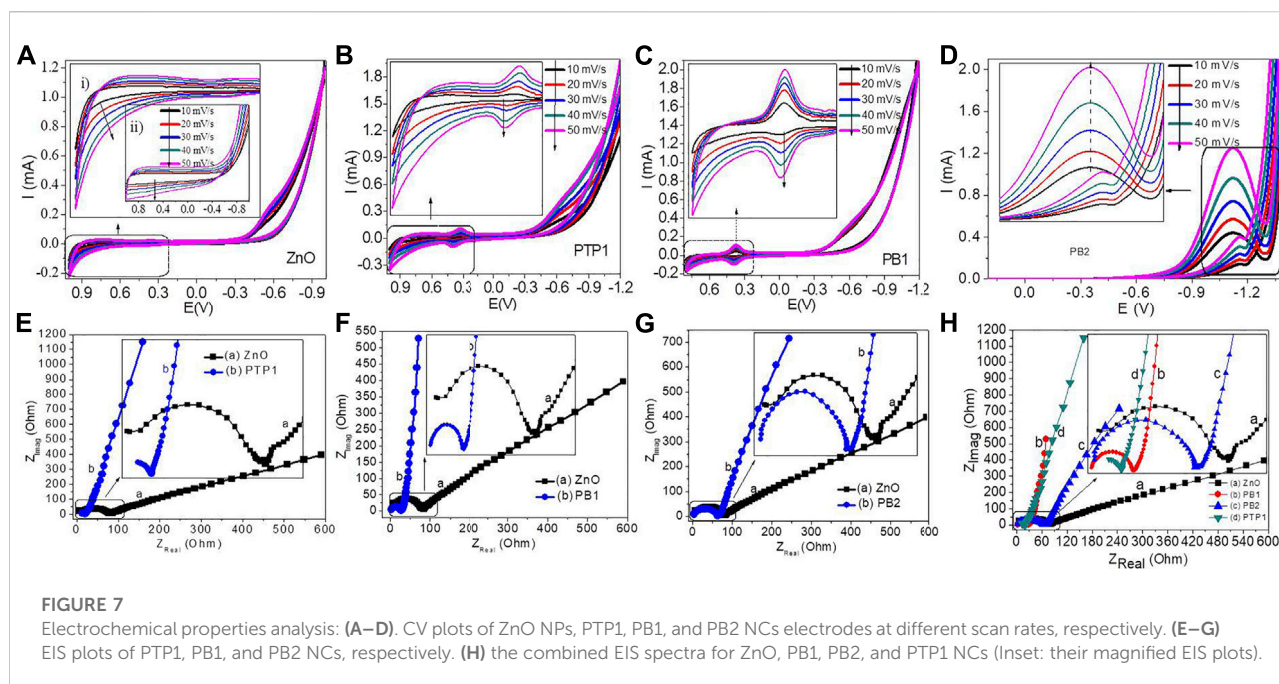
crystallographic orientation (Figures 6D–F) (Penn, 1998; Zhang et al., 2010) and assist the electron transfer from a more negative CB Fermi level to a less negative one and holes from a less negative VB Fermi level to a more negative one (Zeng et al., 2017). For PTP1 NC, the d-spacing value, 0.28 nm, is consistent with that of the (002) plane of ZnO NPs, and 0.34 nm d-spacing corresponds to the (221) plane of α-Mn_2O_3 (Liu X et al., 2016; Zhao et al., 2018). The lattice fringes result of 0.368 nm agrees with the (012) crystal plane of Fe_2O_3 (Yan et al., 2011) (Figure 6D). The lattice fringes result of 0.343 nm was consistent with the Mn_2O_3 [(221) plane], as shown in Figure 6F.

The detected stacking faults on the inverse fast Fourier transmission image reveal the porous properties of the NCs (Figures 6D–F inset). The measured d-spacing (from SAED patterns) values for all PTP1, PB1, and PB2 NCs also matched with the hexagonal wurtzite structure of ZnO. Additional uneven spots observed on the PTP1 and PBP1 NCs are reasonably due to Fe_2O_3 or/and Mn_2O_3 (Tzitzios et al., 2007). The diffraction spots present exactly on the SAED ring indicate the crystallinity of ZnO NPs. The outside spots are undoubtedly for Fe_2O_3 or/and Mn_2O_3 (Zhai et al., 2012). None of the spots was detected in PTP1 NC, indicating the less crystalline properties of the sample. Furthermore, unlike that of PTP1 and PB1 NCs (Figures 6A, B, respectively), the presence of two different crystallites for PB2 (Figure 6C) showed the presence of two different oxides.

The clarity on the phases of metal oxides has been further achieved through the XPS analysis. The high-resolution spectrum XPS analysis for ZnO NPs, PB1, PB2, and PTP1 NCs is presented in Supplementary Figures S2A–D

inset. The 2p, 3s, 3p, and 3d chemical states of Zn; 2p and 3p of iron; 2p and 3p of manganese; and O 1s and 2s of oxygen were predicted from the composition of ZnO, Fe_2O_3, and Mn_2O_3. A typical XPS ZnO NPs spectrum is presented in Supplementary Figure S2A, indicating the existence of O 1s, C 1s, and Zn 2p elements. The high-resolution spectrum of the ZnO NPs peaks at ~1,045.2 and 1,022.0 eV are complied with the electron binding energies of $2p_{1/2}$ and Zn $2p_{3/2}$, respectively (Mao, 2019).

Supplementary Figure S2B shows the spectrum of the PB1 NC validating the existence of Zn 2p, Fe 2p, O 1s, and C 1s chemical states. From the high-resolution spectrum of Fe, the peaks at the binding energies of 711 and 725 eV are consistent with Fe's $2p_{1/2}$ and $2p_{3/2}$ chemical states, and a similar result was reported in the past (Wu et al., 2010). Furthermore, the accompanying of these peaks by satellite structures (as shown by arrows, 720 and 730 eV) confirms the exact electronic structures of Fe^{3+} (Fe_2O_3) (Liu et al., 2012; Wu et al., 2010).

The XPS spectrum (wide scan survey) of PB2 NC, which approves the existence of Zn 2p, Mn 2p, O1s, and C 1s chemical states, is shown in Supplementary Figure S2C. The high-resolution Mn 2p orbital region corroborates the chemical states of Mn $2p_{3/2}$ and Mn $2p_{1/2}$ that exist at binding energies of 641.1 and 653.2 eV, respectively (Saravanan et al., 2015). The approximate splitting energy between Mn $2p_{3/2}$ and Mn $2p_{1/2}$, 12.1 eV, is a characteristic value for Mn_2O_3 (Mn^{3+}) (Yang et al., 2014). Supplementary Figure S2D approves the existence of Zn 2p, Mn 2p, Fe 2p, O 1s, and C 1s chemical states in the PTP1 NC. The Mn $2p_{1/2}$ and Mn $2p_{3/2}$ peaks have appeared at binding energies of 641.1 and 653.7 eV, whereas the Fe $2p_{3/2}$ and Fe $2p_{1/2}$ peaks have appeared at binding energies of 711.3 and 722.3 eV.
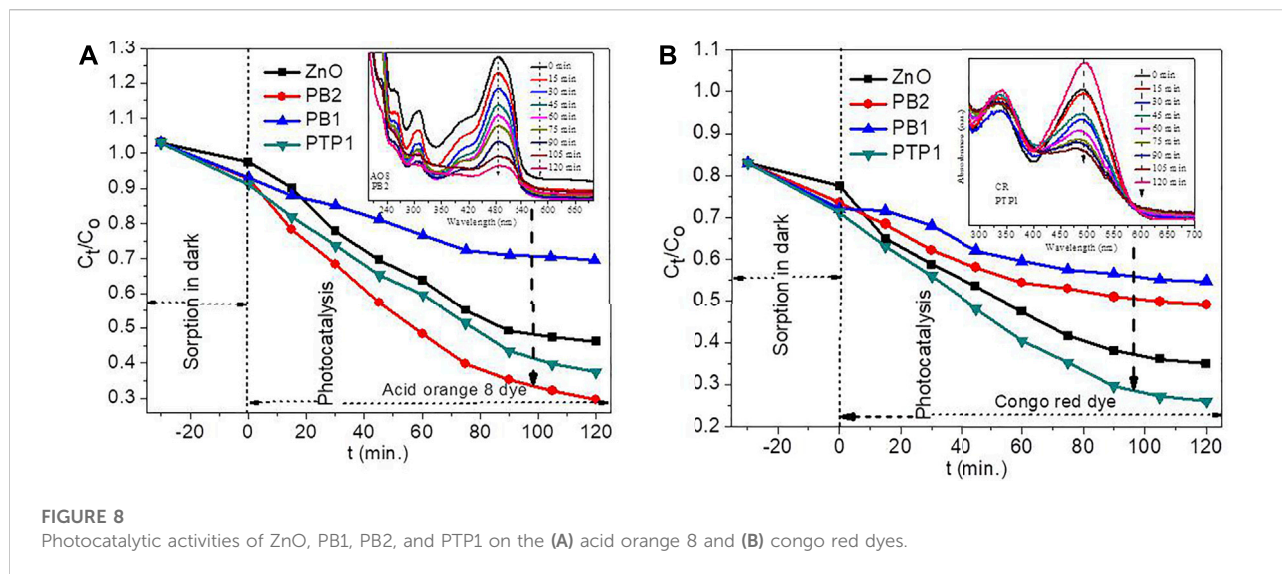
FIGURE 8
Photocatalytic activities of ZnO, PB1, PB2, and PTP1 on the **(A)** acid orange 8 and **(B)** congo red dyes.

The binding energies of the Zn 2p state in PB1, PB2, and PTP1 NCs revealed a slight shift than ZnO peaks, indicating the occurrence of and an e^- transfer from the more negative ZnO Fermi level less negative of Mn_2O_3 or/and Fe_2O_3 Fermi level (Hu et al., 2011; Liu et al., 2012).

The electrochemical features of NPs and NCs have been examined *via* CV and EIS analytical techniques. The CV curves of these ZnO NPs and PB1, PB2, and PTP1 NCs at various scan rates are given in Figures 7A–D. For ZnO NPs, a peak current increase was detected as the scan rate increased without the appearance of reduction–oxidation peaks (Figure 7A) [see also the enlarged ZnO NPs electrode image for modified (inset i) and unmodified (inset ii)]. For PTP1, increasing the scan rate results in a slight rise in the reduction–oxidation peak current (Figure 7B). In PTP1 NC, the observed quick and reversible redox reaction is attributed to the creation of local heterojunctions. Furthermore, this reaction is also associated with the porosity of the NCs, as confirmed by the BET and SEM analyses. The coupling and porous properties of the NCs allow for quick intercalation and de-intercalation processes of the proton (Gopinathan et al., 2015; Liu et al., 2019; Zhang et al., 2011). The small peak potential difference ($\Delta E_{a,c}$) of the anodic (E_{pa}) (+0.401 V) and cathodic peaks (E_{pc}) (+0.323 V) confirms the ability of the PTP1 NC to be reversible.

Figure 7C shows the CV plots of PB1 NC at various scan rates. For PB1 NC, a small increase in the peak current was observed, with an increase in the scan rate, but with the appearance of a pair of redox peaks, unlike that of ZnO. The observed small redox peak potential difference (ΔE) between anodic +0.391 V and +0.370 V potential, 0.021 V, indicates the fast and more reversible ability of the PB1 NC. As indicated, this is also due to the porous nature of the NCs and the formation of local heterojunctions, which reveals a non-restricted path for

e-transfer. In addition to the porosity and heterojunction formation between the metal oxides, these reversible oxidation–reduction peaks that have not appeared on the ZnO NPs are the result of the transformation of Fe^{2+} and Fe^{3+} (Eq. 1) (Wang et al., 2018).

$$Fe(OH)_2 + OH^- \leftrightarrow FeOOH + H_2O + e^- \qquad (1)$$

The presumable mechanism of this redox peak is associated with the reaction of Mn^{3+}/Mn^{4+} (Eq. 2) (Han et al., 2020). The effect of the scan rate on the redox peak current increment has also been detected. The fitted linear relationships between the redox peak current (I_p) and the scan rate (υ) for PTP1, PB1, and PB2 NCs are shown in Supplementary Figures S3A–C, respectively. Depending on the coefficient of determination (R^2) value, for PTP1 and PB2, good linearity between υ and I_p was obtained within 10–50 mV/s. The fitting of their linear curve confirms the presence of a surface-confined electrochemical process (Tang et al., 2008). The well-fit of the linear curve also confirms the domination of adsorption types of the electrocatalytic process. The non-fitting of the PB1 linear plot justifies the diffusion type of the electrocatalytic process (Tang et al., 2008; Suresh et al., 2014).

Nyquist plots were utilized to understand the electrochemical properties of ZnO and NCs. Figures 7E–G shows the EIS plots of PTP1, PB1, and PB2 NCs in contrast to ZnO NPs. The semicircular diameter on the Nyquist plot is equivalent to the electrolyte and modified electrode interface e^- transfer resistance (R_{ct}) (Xie et al., 2014). As seen in Figure 7H, the semicircular diameter of PTP1 NC is significantly smaller than the ZnO NPs and two binary NCs. It indicates that PTP1 NC has a greater charge transfer capacity and a higher photoelectron–hole pair separation performance.

$$Mn[Mn]O_3 + OH^- \leftrightarrow Mn^{4+} + [Mn^{3+}]OH^-O_3 + e^- \qquad (2)$$

SCHEME 2
Possible proposed degradation mechanism: the **(A)**. Straddling, **(B)** staggered, and **(C)** broken gap band alignment for semiconductor heterojunction, **(D)** band energy, and positions of Fe_2O_3, ZnO, and, Mn_2O_3 NPs before the local junction, **(E)** after the junctions.
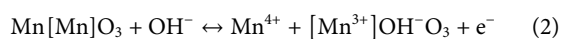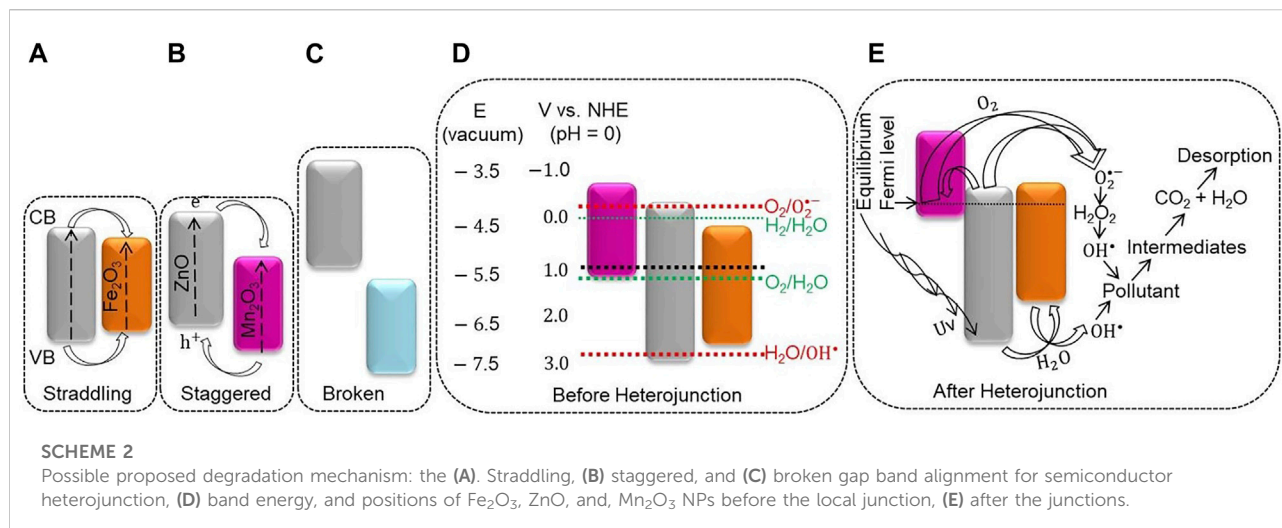
The descending sequence of R_{ct} values of ZnO NPs and PB1, PB2, and PTP1 NCs was $65 > 25 > 61 > 7\Omega$, respectively. These results revealed that the charge transfer inclination is in the order of PTP1 > PB1 > PB2 > ZnO. This improved conductivity of the NCs is also attributed to the porosity and creation of a local junction between ZnO NPs and Fe_2O_3/Mn_2O_3 (Khan et al., 2016; Y. Liu et al., 2014). Additionally, higher charge transferability was observed by increasing the local junction to the ternary (PTP1). As described in Suryavanshi and Rajpure, 2018, this charge transfer capability is also attributed to the negative band edge location of the NCs than in that of ZnO NPs, indicating greater e^-/h^+ recombination hindrance ability. The linear portion at lower frequencies, also known as Warburg resistance, is associated with the diffusion of ions from the electrolyte solution to the modified electrode surface (Kasap et al., 2019).

Photocatalytic activities and mechanisms

Figures 8A,B show the photodegradation activities of ZnO NPs and PB1, PB2, and PTP1 NCs. Except for PB2 NC on the indirect Kubelka–Munk plot, the UV–vis–DRS (Figure 4C) analysis confirms the non-existence of noticeable bandgap change between ZnO NPs and NCs. Therefore, the UV 125 W mercury vapor lamp has been used for this study. The absence of a noticeable bandgap change shows the non-existence of Fe^{3+} or Mn^{3+} inclusion in the crystalline lattice of ZnO. The absence of a noticeable bandgap further confirms the presence of exclusively local heterojunction between ZnO and Fe_2O_3 or/and Mn_2O_3 (Maya-Treviño et al., 2015; Lachheb et al., 2017). Actually, according to Pearson's hard/soft acids/bases theory, hard Lewis acids (such as Mn and Fe) cannot diffuse into the host lattice; instead, they are adsorbed on the surface and oxidize to form a hybrid upon calcination (Buonsanti and Milliron, 2013;

H. Hu et al., 2018). The degradation experiment was conducted using the AO8 (Figure 8A) and CR (Figure 8B) dyes. A small percentage of adsorption occurred in the adsorption/desorption equilibration in the dark. The ZnO and PB2 showed decent photocatalytic activities on the AO8 dye. The obtained rate constant k values for ZnO and PB2 have been deduced to be 0.0058 min^{-1} and 0.0087 min^{-1}, respectively. In addition, ZnO also showed good photocatalytic activities on the CR dye with the rate constant k value of 0.0056 min^{-1}. The k values are obtained from the linear pseudo first-order kinetics linear plot (Ln C_t/C_o verses t) (Supplementary Equation S1). The good photocatalytic activities of ZnO NPs without recombination may be associated with some defects (vacancy) that prevent the e^-/h^+ recombination.

The photocatalytic activity of PB2 on the AO8 dye is still better than PTP1 NC, which is probably due to the formation of a suitable staggered type heterojunction (Scheme 2B). In the staggering gap type of heterojunction, the electrons are transferred from ZnO's more negative CB potential to the less negative CB potential of Mn_2O_3. The holes are transferred from the more positive VB potential of Mn_2O_3 to the less positive VB potential of ZnO (Jiamprasertboon et al., 2019). Consequently, the e^- and h^+ separation has been raised, enhancing the degradation efficiency significantly (Marschall, 2014). The PB2 NC also showed a redshift on the indirect Kubelka–Munk plot (Figure 4C), which assists with the broad-spectrum light absorption efficiency (Hu and Yang, 2017). However, the photocatalytic activity of PB2 on the CR dye was not appreciable. The typical anionic diazo CR dye has a highly stable structure, making it difficult to degrade (Lei et al., 2017).

The photocatalytic activities of PB1 NC on both CR and AO8 dyes are inadequate. This inadequacy is maybe because of the enhancement of the e^-–h^+ recombination, probably due to

the formation of a straddling gap type of the heterojunction (Xu et al., 2018), as shown in Scheme 2A. In the straddling gap type of heterojunction, the e^- transferred from the more negative CB potential of ZnO to the lower CB potential of Fe_2O_3. The holes migrate from ZnO's less negative VB potential to the more negative VB potential of Fe_2O_3 (Jiamprasertboon et al., 2019). Thus, the e^- and h^+ were collected and recombined in Fe_2O_3, weakening the photocatalytic efficiency (Marschall, 2014). The band edge positions of the broken gap heterojunction have noticeable variation (Scheme 2C). This greater energy difference requires higher motive energy to transfer the photo-induced electrons and holes (Jiamprasertboon et al., 2019). The PTP1 NC has greater SAS and better charge transfer capability based on the characterization analysis. Unlike ZnO NPs and the binary NCs, the PTP1 NC has an appreciable photodegradation activity toward CR and AO8 dyes. The obtained k values for AO8 and CR dyes were 0.0056 min^{-1} and 0.0072 min^{-1}, respectively.

Semiconductors have a characteristic band energy that absorbs a precise frequency of light, although their band edge position depends on the surface charge (Beranek, 2011). For semiconductors, owning more negative CB than the H^+/H_2 reduction potential and more positive VB than the O_2/H_2O reduction potential is crucial for pollutant degradation (Hoffmann et al., 1995). Before the heterojunction, from the electron affinity aspect, the redox potentials of ZnO, Fe_2O_3 (Ganguly et al., 2015), and Mn_2O_3 (P. Li et al., 2019; Saravanan et al., 2014) were designed as shown in Scheme 2D. Furthermore, an electrochemical analysis is significant to knowing metal oxides' exact band edge position (Beranek, 2011). From the CV and EIS analyses, it is found that the PTP1 NC shows a quick and reversible redox reaction that shows the existence of better charge transfer synergy (Figures 7B, E,). The presence of a good charge transfer property shows the formation of heterojunctions/local contacts between the metal oxides, which has a noticeable influence on diminishing the e^-/h^+ recombination. After the heterojunction, based on the study results and reviews (Zhang et al., 2011; Lachheb et al., 2017), a possible proposed degradation mechanism of PTP1 NC was suggested, as shown in Scheme 2E.

Conclusion

Improvement in the synthesis techniques and their optimum properties is the up-to-date global need for industrially scalable applications. The sol–gel-based solution combustion synthesis approach is easy, time-/energy-efficient, and creates regularly ordered porous materials that have significance in the ion-/mass-transport phenomenon. Furthermore, the approach also yields a decent heterojunction once optimized *via* the hard/soft acids/bases

theory. Forming a heterojunction also tunes the crucial properties of the materials, thus boosting the photocatalytic ability through charge transfer or/and synergistic roles. From the stability investigation results, the calcination temperature of 500 C was ideal. The XRD and HRTEM techniques confirmed the nanoscale size of the NPs and NCs. The approximate average crystallite size of the parent ZnO NPs and ternary NCs is 60 and 10 nm, respectively. The mesoporous nature of the materials is confirmed from the SEM image and BET analysis. The approximate specific surface area from the BET analysis for ZnO NPs and ternary NCs is 2 and 24 m^2/g, respectively. The approximate average pore size distribution of the NPS and NCs is between 10 and 45 nm. The elemental composition has been confirmed from HRTEM, XPS, and EDX studies. The electrical impedance spectroscopy and cyclic voltammetry studies confirmed an improved charge transfer for binary and ternary NCs, compared to ZnO NPs. The NC materials showed better dye degradation properties than ZnO.

Data availability statement

The original contributions presented in the study are included in the article/Supplementary Material; further inquiries can be directed to the corresponding author.

Author contributions

Writing—original draft, Writing—review and editing, and Investigation by BA.

Funding

Conflict of interest

The authors declare that the research was conducted in the absence of any commercial or financial relationships that could be construed as a potential conflict of interest.

Publisher's note

All claims expressed in this article are solely those of the authors and do not necessarily represent those of their

Supplementary material

The Supplementary Material for this article can be found online at: https://www.frontiersin.org/articles/10.3389/fctls.2022. 950384/full#supplementary-material

References

Adeleye, A. S., Conway, J. R., Garner, K., Huang, Y., Su, Y., and Keller, A. A. (2016). Engineered nanomaterials for water treatment and remediation: costs, benefits, and applicability. *Chem. Eng. J.* 286, 640–662. doi:10.1016/j.cej.2015.10.105

Anžlovar, A., Kogej, K., Crnjak Orel, Z., and Žigon, M. (2011). Polyol mediated nano size zinc oxide and nanocomposites with poly(methyl methacrylate). *Express Polym. Lett.* 5 (7), 604–619. doi:10.3144/expresspolymlett.2011.59

Beranek, R. (2011). Photo)electrochemical methods for the determination of the band edge positions of TiO_2 based nanomaterials. *Adv. Phys. Chem.* 1–20. doi:10. 1155/2011/786759

Boningari, T., Inturi, S. N. R., Suidan, M., and Smirniotis, P. G. (2018). Novel one-step synthesis of nitrogen-doped TiO_2 by flame aerosol technique for visible-light photocatalysis: effect of synthesis parameters and secondary nitrogen (N) source. *Chem. Eng. J.* 350, 324–334. doi:10.1016/j.cej.2018.05.122

Broekhoff, J. C. P., and Issue, C. (1979). Mesopore determination from nitrogen sorption isotherms: fundamentals, scope, limitations. *Stud. Surf. Sci. Catal.* 3, 663–684. doi:10.1016/S0167-2991(09)60243-3

Buonsanti, R., and Milliron, D. J. (2013). Chemistry of doped colloidal nanocrystals. *Chem. Mat.* 25 (8), 1305–1317. doi:10.1021/cm304104m

Chen, P., Tai, Y., Fang, Q., Xu, D., Gao, Y., and Cheng, J. (2021). Solution combustion synthesis of ternary Ni/WC/C composites with efficient electrocatalytic oxygen reduction performance. *RSC Adv.* 11 (61), 38718–38726. doi:10.1039/ D1RA06884A

Cochran, E. A., Woods, K. N., Johnson, D. W., Page, C. J., and Boettcher, S. W. (2019). Unique chemistries of metal-nitrate precursors to form metal-oxide thin films from solution: materials for electronic and energy applications. *J. Mat. Chem. A Mat.* 7 (42), 24124–24149. doi:10.1039/C9TA07727H

Dai, Y., Tang, Q., Zhang, Z., Yu, C., Li, H., Xu, L., et al. (2018). Enhanced mechanical, thermal, and UV-shielding properties of poly(vinyl alcohol)/ metal–organic framework nanocomposites. *RSC Adv.* 8 (67), 38681–38688. doi:10.1039/C8RA07143H

Deganello, F., and Tyagi, A. K. (2018). Solution combustion synthesis, energy and environment: best parameters for better materials. *Prog. Cryst. Growth Charact. Mater.* 64 (2), 23–61. doi:10.1016/j.pcrysgrow.2018.03.001

Deng, H., Fei, X., Yang, Y., Fan, J., Yu, J., Cheng, B., et al. (2021). S-scheme heterojunction based on p-type ZnMn2O4 and n-type ZnO with improved photocatalytic CO_2 reduction activity. *Chem. Eng. J.* 409, 127377. doi:10.1016/j. cej.2020.127377

Dhal, J. P., Mishra, B. G., and Hota, G. (2015). Hydrothermal synthesis and enhanced photocatalytic activity of ternary Fe_2O_3/$ZnFe_2O_4$/ZnO nanocomposite through cascade electron transfer. *RSC Adv.* 5 (71), 58072–58083. doi:10.1039/ C5RA05894E

Fatehah, M. O., Aziz, H. A., and Stoll, S. (2014). Stability of ZnO nanoparticles in solution. Influence of pH, dissolution, aggregation and disaggregation effects. *J. Coll. Sci. Biotechnol.* 3 (1), 75–84. doi:10.1166/jcsb.2014.1072

Ganguly, A., Anjaneyulu, O., Ojha, K., and Ganguli, A. K. (2015). Oxide-based nanostructures for photocatalytic and electrocatalytic applications. *CrystEngComm* 17 (47), 8978–9001. doi:10.1039/C5CE01343G

Gao, Y., Meng, F., Li, X., Wen, J. Z., and Li, Z. (2016). Factors controlling nanosized Ni–Al_2O_3 catalysts synthesized by solution combustion for slurry-phase CO methanation: the ratio of reducing valences to oxidizing valences in redox systems. *Catal. Sci. Technol.* 6 (21), 7800–7811. doi:10.1039/C6CY01603K

Gómez-Pastora, J., Dominguez, S., Bringas, E., Rivero, M. J., Ortiz, I., and Dionysiou, D. D. (2017). Review and perspectives on the use of magnetic nanophotocatalysts (MNPCs) in water treatment. *Chem. Eng. J.* 310, 407–427. doi:10.1016/j.cej.2016.04.140

González-Cortés, S. L., and Imbert, F. E. (2013). Fundamentals, properties and applications of solid catalysts prepared by solution combustion synthesis (SCS). *Appl. Catal. A General* 452, 117–131. doi:10.1016/j.apcata.2012.11.024

Gopinathan, E., Viruthagiri, G., Shanmugam, N., and Sathiya priya, S. (2015). Optical, surface analysis and antibacterial activity of ZnO–CuO doped cerium oxide nanoparticles. *Optik* 126 (24), 5830–5835. doi:10.1016/j.ijleo.2015.09.014

Han, H., Sial, Q. A., Kalanur, S. S., and Seo, H. (2020). Binder assisted self-assembly of graphene oxide/Mn_2O_3 nanocomposite electrode on Ni foam for efficient supercapacitor application. *Ceram. Int.* 46 (10), 15631–15637. doi:10. 1016/j.ceramint.2020.03.111

Hoffmann, M. R., Martin, S. T., Choi, W., and Bahnemann, D. W. (1995). Environmental applications of semiconductor photocatalysis. *Chem. Rev.* 95 (1), 69–96. doi:10.1021/cr00033a004

Hu, H., He, H., Zhang, J., Hou, X., and Wu, P. (2018). Optical sensing at the nanobiointerface of metal ion-optically-active nanocrystals. *Nanoscale* 10 (11), 5035–5046. doi:10.1039/c8nr00350e

Hu, W., and Yang, J. (2017). Two-dimensional van der Waals heterojunctions for functional materials and devices. *J. Mat. Chem. C Mat.* 5 (47), 12289–12297. doi:10. 1039/c7tc04697a

Hu, Y., Qian, H., Liu, Y., Du, G., Zhang, F., Wang, L., et al. (2011). A microwave-assisted rapid route to synthesize ZnO/ZnS core–shell nanostructures via controllable surface sulfidation of ZnO nanorods. *CrystEngComm* 13 (10), 3438. doi:10.1039/c1ce05111c

Janotti, A., and Van de Walle, C. G. (2009). Fundamentals of zinc oxide as a semiconductor. *Rep. Prog. Phys.* 72 (12), 126501. doi:10.1088/0034-4885/72/12/ 126501

Jassby, D., Farner Budarz, J., and Wiesner, M. (2012). Impact of aggregate size and structure on the photocatalytic properties of TiO_2 and ZnO nanoparticles. *Environ. Sci. Technol.* 46 (13), 6934–6941. doi:10.1021/es202009h

Jiamprasertboon, A., Kafizas, A., Sachs, M., Ling, M., Alotaibi, A. M., Lu, Y., et al. (2019). Heterojunction α-Fe_2O_3/ZnO films with enhanced photocatalytic properties grown by aerosol-assisted chemical vapour deposition. *Chemistry* 25, 11337–11345. doi:10.1002/chem.201902175

Kasap, S., Kaya, I. I., Repp, S., and Erdem, E. (2019). Superbat: battery-like supercapacitor utilized by graphene foam and zinc oxide (ZnO) electrodes induced by structural defects. *Nanoscale Adv.* 1 (7), 2586–2597. doi:10.1039/C9NA00199A

Khan, S. B., Ahmed, M. S., and Asiri, A. M. (2016). Amperometric sensor for ascorbic acid using a gold electrode modified with ZnO@SiO_2 nanospheres. *New J. Chem.* 40 (10), 8438–8443. doi:10.1039/C6NJ00115G

Khort, A., Hedberg, J., Mei, N., Romanovski, V., Blomberg, E., and Odnevall, I. (2021). Corrosion and transformation of solution combustion synthesized Co, Ni and CoNi nanoparticles in synthetic freshwater with and without natural organic matter. *Sci. Rep.* 11 (1), 7860. doi:10.1038/s41598-021-87250-7

Kim, S. J., Yoon, S., and Kim, H. J. (2014). Review of solution-processed oxide thin-film transistors. *Jpn. J. Appl. Phys. (2008).* 53 (2S), 02BA02. doi:10.7567/JJAP. 53.02BA02

Kumar, P., Kim, K.-H., Kwon, E. E., and Szulejko, J. E. (2016). Metal–organic frameworks for the control and management of air quality: advances and future direction. *J. Mat. Chem. A Mat.* 4 (2), 345–361. doi:10.1039/C5TA07068F

Kumar, S., Krishnakumar, B., Sobral, A. J. F. N., and Koh, J. (20192018). Bio-based (chitosan/PVA/ZnO) nanocomposites fi lm : Thermally stable and photoluminescence material for removal of organic dye. *Carbohydr. Polym.* 205, 559–564. doi:10.1016/j.carbpol.2018.10.108

Lachheb, H., Ajala, F., Hamrouni, A., Houas, A., Parrino, F., and Palmisano, L. (2017). Electron transfer in ZnO–Fe_2O_3 aqueous slurry systems and its effects on visible light photocatalytic activity. *Catal. Sci. Technol.* 7 (18), 4041–4047. doi:10. 1039/C7CY01085K

Lam, S.-M., Lim, C.-L., Sin, J.-C., Zeng, H., Lin, H., and Li, H. (2021). Facile synthesis of MnO2/ZnO coated on cotton fabric for boosted antimicrobial, self-cleaning and photocatalytic activities under sunlight. *Mater. Lett.* 305, 130818. doi:10.1016/j.matlet.2021.130818

Lei, C., Pi, M., Jiang, C., Cheng, B., and Yu, J. (2017). Synthesis of hierarchical porous zinc oxide (ZnO) microspheres with highly efficient adsorption of Congo red. *J. Colloid Interface Sci.* 490, 242–251. doi:10.1016/j.jcis.2016.11.049

Li, N., Li, R., Zhao, J., Liang, L., Yu, Y., Kong, L., et al. (2020). Multi-interface $Mn_3O_4@ZnO/TiO_2$ with controllable charge transfer routes for highly selective denitrification under ultrasonic-assisted visible light photocatalysis. *Chem. Eng. J.* 394, 124997. doi:10.1016/j.cej.2020.124997

Li, P., Zhao, R., Chen, H., Wang, H., Wei, P., Huang, H., et al. (2019). Recent advances in the development of water oxidation electrocatalysts at mild pH. *Small* 15 (13), 1805103–1805127. doi:10.1002/smll.201805103

Liu, J., Xu, T., Sun, X., Bai, J., and Li, C. (2019). Preparation of stable composite porous nanofibers carried SnOx-ZnO as a flexible supercapacitor material with excellent electrochemical and cycling performance. *J. Alloys Compd.* 807, 151652. doi:10.1016/j.jallcom.2019.151652

Liu, Y., Pang, H., Wei, C., Hao, M., Zheng, S., and Zheng, M. (2014). Mesoporous ZnO-NiO architectures for use in a high-performance nonenzymatic glucose sensor. *Microchim. Acta* 181 (13–14), 1581–1589. doi:10.1007/s00604-014-1275-9

Liu, Y., Yu, L., Hu, Y., Guo, C., Zhang, F., David, W., et al. (2012). A magnetically separable photocatalyst based on nest-like γ-Fe₂O₃/ZnO double-shelled hollow structures with enhanced photocatalytic activity. *Nanoscale* 4 (1), 183–187. doi:10.1039/C1NR11114K

Liu, B, B., You, Y., Zhang, H., Wu, H., Jin, J., and Liu, H. (2016). Synthesis of ZnO nano-powders via a novel PVA-assisted freeze-drying process. *RSC Adv.* 6 (111), 110349–110355. doi:10.1039/C6RA24154A

Liu, J, J., He, J., Wang, L., Li, R., Chen, P., Rao, X., et al. (2016). NiO-PTA supported on ZIF-8 as a highly effective catalyst for hydrocracking of Jatropha oil. *Sci. Rep.* 6 (1), 23667. doi:10.1038/srep23667

Liu, X, X., Ye, L., Liu, S., Li, Y., and Ji, X. (2016). Photocatalytic reduction of CO_2 by ZnO micro/nanomaterials with different morphologies and ratios of {0001} facets. *Sci. Rep.* 6 (1), 38474. doi:10.1038/srep38474

Mao, N. (2019). Investigating the Heterojunction between ZnO/Fe_2O_3 and g-C3N4 for an Enhanced Photocatalytic H_2 production under visible-light irradiation. *Sci. Rep.* 9 (1), 12383. doi:10.1038/s41598-019-48730-z

Marschall, R. (2014). Semiconductor composites : strategies for enhancing charge carrier separation to improve photocatalytic activity. *Adv. Funct. Mat.* 24, 2421–2440. doi:10.1002/adfm.201303214

Maya-Treviño, M. L., Villanueva-Rodríguez, M., Guzmán-Mar, J. L., Hinojosa-Reyes, L., and Hernández-Ramírez, A. (2015). Comparison of the solar photocatalytic activity of $ZnO–Fe_2O_3$ and ZnO–Fe 0 on 2, 4-D degradation in a CPC reactor. *Photochem. Photobiol. Sci.* 14 (3), 543–549. doi:10.1039/C4PP00274A

Nagvenkar, A. P., Perelshtein, I., Piunno, Y., Mantecca, P., and Gedanken, A. (2019). Sonochemical one-step synthesis of polymer-capped metal oxide nanocolloids: Antibacterial activity and cytotoxicity. *ACS Omega* 4 (9), 13631–13639. doi:10.1021/acsomega.9b00181

Nersisyan, H. H., Lee, J. H., Ding, J.-R., Kim, K.-S., Manukyan, K. V., and Mukasyan, A. S. (2017). Combustion synthesis of zero-one-two- and three-dimensional nanostructures: current trends and future perspectives. *Prog. Energy Combust. Sci.* 63, 79–118. doi:10.1016/j.pecs.2017.07.002

Novitskaya, E., Kelly, J. P., Bhaduri, S., and Graeve, O. A. (2021). A review of solution combustion synthesis: an analysis of parameters controlling powder characteristics. *Int. Mater. Rev.* 66 (3), 188–214. doi:10.1080/09506608.2020.1765603

Nsib, M. F., Naffati, N., Rayes, A., Moussa, N., and Houas, A. (2015). Effect of some operational parameters on the hydrogen generation efficiency of Ni-ZnO/PANI composite under visible-light irradiation. *Mater. Res. Bull.* 70, 530–538. doi:10.1016/j.materresbull.2015.04.067

Parler, C. M., Ritter, J. A., and Amiridis, M. D. (2001). Infrared spectroscopic study of sol–gel derived mixed-metal oxides. *J. Non-Crystalline Solids* 279 (2–3), 119–125. doi:10.1016/S0022-3093(00)00401-4

Penn, R. L., and Banfield, J. F. (1998). Imperfect oriented attachment: Dislocation generation in defect-free nanocrystals. *Science* 281 (5379), 969–971. doi:10.1126/science.281.5379.969

Pype, M., Lawrence, M. G., Keller, J., and Gernjak, W. (2016). Reverse osmosis integrity monitoring in water reuse: The challenge to verify virus removal – a review. *Water Res.* 98, 384–395. doi:10.1016/j.watres.2016.04.040

Radhamani, A. V., Shareef, K. M., and Rao, M. S. R. (2016). ZnO@MnO₂ core–shell nanofiber cathodes for high performance asymmetric supercapacitors. *ACS Appl. Mat. Interfaces* 8 (44), 30531–30542. doi:10.1021/acsami.6b08082

Rosman, N., Wan Salleh, W. N., Aziz, F., Ismail, A. F., Harun, Z., Bahri, S. S., et al. (2019). Electrospun nanofibers embedding $ZnO/Ag_2CO_3/Ag_2O$ heterojunction photocatalyst with enhanced photocatalytic activity. *Catalysts* 9 (7), 565. doi:10.3390/catal9070565

Saravanan, R., Gupta, V. K. K., Narayanan, V., and Stephen, A. (2014). Visible light degradation of textile effluent using novel catalyst $ZnO/γ-Mn_2O_3$. *J. Taiwan Inst. Chem. Eng.* 45 (4), 1910–1917. doi:10.1016/j.jtice.2013.12.021

Saravanan, R., Khan, M. M., Gupta, V. K., Mosquera, E., Gracia, F., Narayanan, V., et al. (2015). $ZnO/Ag/Mn_2O_3$ nanocomposite for visible light-induced industrial textile effluent degradation, uric acid and ascorbic acid sensing and antimicrobial activity. *RSC Adv.* 5 (44), 34645–34651. doi:10.1039/C5RA02557E

Shah, A. H., Manikandan, E., Basheer Ahamed, M., Ahmad Mir, D., and Ahmad Mir, S. (2014). Antibacterial and Blue shift investigations in sol–gel synthesized CrxZn1−xO Nanostructures. *J. Luminescence* 145, 944–950. doi:10.1016/j.jlumin.2013.09.023

Sigoli, F. A., Davolos, M. R., and Jafelicci, M. (1997). Morphological evolution of zinc oxide originating from zinc hydroxide carbonate. *J. Alloys Compd.* 262–263, 292–295. doi:10.1016/S0925-8388(97)00404-0

Singh, R., and Dutta, S. (2019). The role of pH and nitrate concentration in the wet chemical growth of nano-rods shaped ZnO photocatalyst. *Nano-Structures Nano-Objects* 18, 100250. doi:10.1016/j.nanoso.2019.01.009

Srinivasa, N., Hughes, J. P., Adarakatti, P. S., Rowley-Neale, S. J., and Banks, C. E. (2021). Facile synthesis of Ni/NiO nanocomposites: the effect of Ni content in NiO upon the oxygen evolution reaction within alkaline media. *RSC Adv.* 11 (24), 14654–14664. doi:10.1039/D0RA10597J

Suresh, R., Giribabu, K., Manigandan, R., Stephen, A., and Narayanan, V. (2014). Fabrication of Ni–Fe₂O₃ magnetic nanorods and application to the detection of uric acid. *RSC Adv.* 4 (33), 17146. doi:10.1039/c4ra00725e

Suryavanshi, R. D., and Rajpure, K. Y. (2018). Spray deposited Fe_2O_3 and stratified Fe_2O_3/ZnO novel photoelectrode for photoelectrocatalytic degradation of benzoic acid under solar light illumination. *J. Photochem. Photobiol. A Chem.* 357, 72–80. doi:10.1016/j.jphotochem.2018.02.008

Tang, C.-F., Kumar, S. A., and Chen, S.-M. (2008). Zinc oxide/redox mediator composite films-based sensor for electrochemical detection of important biomolecules. *Anal. Biochem.* 380 (2), 174–183. doi:10.1016/j.ab.2008.06.004

Thommes, M., Kaneko, K., Neimark, A. V., Olivier, J. P., Rodriguez-Reinoso, F., Rouquerol, J., et al. (2015). Physisorption of gases, with special reference to the evaluation of surface area and pore size distribution (IUPAC Technical Report). *Pure Appl. Chem.* 87 (9–10), 1051–1069. doi:10.1515/pac-2014-1117

Tzitzios, V. K., Bakandritsos, A., Georgakilas, V., Basina, G., Boukos, N., Bourlinos, A. B., et al. (2007). Large-scale synthesis, size control, and anisotropic growth of &gamma-Fe₂O₃ nanoparticles: Organosols and hydrosols. *J. Nanosci. Nanotechnol.* 7 (8), 2753–2757. doi:10.1166/jnn.2007.605

Uma, K., Muniranthinam, E., Chong, S., Yang, T. C. K., and Lin, J.-H. (2020). Fabrication of hybrid catalyst ZnO nanorod/α-Fe₂O₃ composites for hydrogen evolution reaction. *Crystals* 10 (5), 356. doi:10.3390/cryst10050356

Wachs, I. E. (1996). Raman and IR studies of surface metal oxide species on oxide supports: supported metal oxide catalysts. *Catal. Today* 27 (3–4), 437–455. doi:10.1016/0920-5861(95)00203-0

Wang, Y., Chen, Z., Lei, T., Ai, Y., Peng, Z., Yan, X., et al. (2018). Hollow NiCo₂S₄ nanospheres hybridized with 3D hierarchical porous rGO/Fe₂O₃ composites toward high-performance energy storage device. *Adv. Energy Mat.* 8 (16), 1703453. doi:10.1002/aenm.201703453

Wu, P., Du, N., Zhang, H., Jin, L., and Yang, D. (2010). Functionalization of ZnO nanorods with γ-Fe₂O₃ nanoparticles: layer-by-layer synthesis, optical and magnetic properties. *Mater. Chem. Phys.* 124 (2–3), 908–911. doi:10.1016/j.matchemphys.2010.08.009

Wu, Z., Wu, W., Yang, S., and Wu, W. (2016). Shape control of inorganic nanoparticles from solution. *Nanoscale* 8 (3), 1237–1259. doi:10.1039/C5NR07681A

Xie, J., Hao, Y. J., Zhou, Z., Meng, X. C., Yao, L., Bian, L., et al. (2014). Fabrication and characterization of ZnO particles with different morphologies for photocatalytic degradation of pentachlorophenol. *Res. Chem. Intermed.* 40 (5), 1937–1946. doi:10.1007/s11164-013-1091-6

Xu, K., Xu, Y., Zhang, H., Peng, B., Shao, H., Ni, G., et al. (2018). The role of Anderson's rule in determining electronic, optical and transport properties of transition metal dichalcogenide heterostructures. *Phys. Chem. Chem. Phys.* 20 (48), 30351–30364. doi:10.1039/C8CP05522J

Yan, W., Fan, H., and Yang, C. (2011). Ultra-fast synthesis and enhanced photocatalytic properties of alpha-Fe_2O_3/ZnO core-shell structure. *Mater. Lett.* 65 (11), 1595–1597. doi:10.1016/j.matlet.2011.03.026

Yang, G., Yan, W., Wang, J., and Yang, H. (2014). Fabrication and formation mechanism of Mn_2O_3 hollow nanofibers by single-spinneret electrospinning. *CrystEngComm* 16 (30), 6907–6913. doi:10.1039/C4CE00521J

Yang, Z., Zong, X. L., Ye, Z., Zhao, B., Wang, Q. L., and Wang, P. (2010). The application of complex multiple forklike ZnO nanostructures to rapid and ultrahigh sensitive hydrogen peroxide biosensors. *Biomaterials* 31 (29), 7534–7541. doi:10.1016/j.biomaterials.2010.06.019

Yuvaraj, S., Fan-Yuan, L., Tsong-Huei, C., and Chuin-Tih, Y. (2003). Thermal decomposition of metal nitrates in air and hydrogen environments. *J. Phys. Chem. B* 107 (4), 1044–1047. doi:10.1021/jp026961c

Zeng, Z., Zhang, W., Arvapalli, D. M., Bloom, B., Sheardy, A., Mabe, T., et al. (2017). A fluorescence-electrochemical study of carbon nanodots (CNDs) in bio- and photoelectronic applications and energy gap investigation. *Phys. Chem. Chem. Phys.* 19 (30), 20101–20109. doi:10.1039/C7CP02875J

Zhai, T., Xie, S., Zhao, Y., Sun, X., Lu, X., Yu, M., et al. (2012). Controllable synthesis of hierarchical ZnO nanodisks for highly photocatalytic activity. *CrystEngComm* 14 (5), 1850. doi:10.1039/c1ce06013a

Zhang, J., Guo, Q., Liu, Y., and Cheng, Y. (2012). Preparation and characterization of Fe_2O_3/Al_2O_3 using the solution combustion approach for chemical looping combustion. *Ind. Eng. Chem. Res.* 51 (39), 12773–12781. doi:10.1021/ie301804c

Zhang, J., Huang, F., and Lin, Z. (2010). Progress of nanocrystalline growth kinetics based on oriented attachment. *Nanoscale* 2 (1), 18–34. doi:10.1039/B9NR00047J

Zhang, J., Liu, X., Wang, L., Yang, T., Guo, X., Wu, S., et al. (2011). Synthesis and gas sensing properties of α-Fe_2O_3 @ ZnO core–shell nanospindles. *Nanotechnology* 22 (18), 185501. doi:10.1088/0957-4484/22/18/185501

Zhao, J., Zhao, Z., Li, N., Nan, J., Yu, R., and Du, J. (2018). Visible-light-driven photocatalytic degradation of ciprofloxacin by a ternary Mn_2O_3/Mn_3O_4/MnO_2 valence state heterojunction. *Chem. Eng. J.* 353 (73), 805–813. doi:10.1016/j.cej.2018.07.163